Nature of the Ti−Ba Interactions on the BaO/TiO$_2$/Al$_2$O$_3$ NO$_x$ Storage System

Stanislava M. Andonova,[†] Göksu S. Şentürk,[†] Emine Kayhan,[†] and Emrah Ozensoy*,[†,‡]

Chemistry Department, Bilkent University, 06800 Bilkent, Ankara, Turkey and Institute of Material Science and Nanotechnology, 06800 Bilkent, Ankara, Turkey

A ternary oxide-based NO$_x$ storage material in the form of BaO/TiO$_2$/γ-Al$_2$O$_3$ was synthesized and characterized. Thermally induced structural changes occurring on the surfaces of the TiO$_2$/γ-Al$_2$O$_3$ and BaO/TiO$_2$/γ-Al$_2$O$_3$ systems were studied in a comparative manner within 300−1273 K via X-ray diffraction (XRD), Raman spectroscopy, scanning electron microscopy (SEM), energy-dispersive X-ray (EDX) spectroscopy, and BET surface area analysis. The surface acidity of the studied oxide systems was also investigated via pyridine adsorption monitored by in-situ Fourier transform infrared (FTIR) spectroscopy. BaO/TiO$_2$/γ-Al$_2$O$_3$ ternary oxide was synthesized by incorporating different loadings of (8−20 wt %) BaO onto the TiO$_2$/γ-Al$_2$O$_3$ support material, which was originally prepared using the sol−gel method. In the TiO$_2$/γ-Al$_2$O$_3$ binary oxide support material, anatase phase exhibited a relatively high thermal stability at $T \leq 1073$ K. The presence of TiO$_2$ domains on the surface of the alumina particles was found to alter the surface acidity of alumina by providing new medium-strength Lewis acid sites. SEM/EDX results indicate that in the BaO/TiO$_2$/γ-Al$_2$O$_3$ system, TiO$_2$ domains present a significant affinity toward BaO and/or Ba(NO$_3$)$_2$ resulting in a strong Ti−Ba interaction and the formation of overlapping domains on the surface. The presence of TiO$_2$ also leads to a decrease in the decomposition temperature of the Ba(NO$_3$)$_2$ phase with respect to the Ti-free Ba(NO$_3$)$_2$/γ-Al$_2$O$_3$ system. Such a destabilization is likely to occur due to a weaker interaction between Ba(NO$_3$)$_2$ and γ-Al$_2$O$_3$ domains in the ternary oxide as well as due to the change in the surface acidity in the presence of TiO$_2$. At relatively high temperatures (e.g., 873−1273 K) formation of complex structures in the form of BaTiO$_3$, Ba$_{1.23}$Al$_{2.46}$Ti$_{5.54}$O$_{16}$, BaTiO$_5$, and/or Ba$_x$Al$_y$Ti$_z$O$_n$ were also observed.

1. Introduction

In the past decade, NO$_x$ storage/reduction (NSR) technology originally developed by Toyota Motor Corporation[1,2] has attracted considerable attention as a promising after treatment technology for catalytic NO$_x$ removal from mobile sources. Numerous efforts[3−5] have been directed toward designing highly active NSR catalysts with long-term durability and improved sulfur tolerance. Various experimental and theoretical studies[6−9] also focused on the properties of the Pt/BaO/γ-Al$_2$O$_3$ NSR catalytic system and its application to diesel-fueled vehicles which operate under excess oxygen. In addition, several detailed surface science studies[10−16] on the NO$_x$ storage capacity and the thermal aging of model NO$_x$ storage materials in the form of BaO/θ-Al$_2$O$_3$/NiAl(100) were also reported in the literature. NSR catalysts function through alternating cycles of lean (abundant in oxygen) and rich (abundant in reductants such as unburned hydrocarbons, H$_2$ and CO) regimes.[17,18] During the lean period, NO$_x$ is oxidized over a noble metal active center (mainly Pt or Pt−Rh) and then stored on a storage compound containing alkaline earth oxides (mainly BaO) in the form of nitrites and nitrates (Ba(NO$_2$)$_2$ and Ba(NO$_3$)$_2$). During the short rich period, NO$_x$ is released from the storage component and successively reduced to N$_2$ on the noble metal sites.

Despite the constant reduction in the sulfur content of the refined fuel in the past decades, sulfur poisoning remains as one of the major causes for catalytic deactivation of the NSR systems.[19−23]

As a support material of the NSR catalysts, TiO$_2$ was found to have a noticeable ability to suppress sulfur deposition.[24] This was associated with the surface acidity of TiO$_2$, inhibiting the adsorption of acidic sulfur species and making the sulfates less stable on the TiO$_2$ compared to other oxide supports. It was also shown that the decomposition temperature of the sulfates on a TiO$_2$ support was lower than that on a γ-Al$_2$O$_3$. However, in order to circumvent some of the unfavorable aspects of pure TiO$_2$ such as the limited thermal stability, low surface area, and poor mechanical properties, its combination with secondary oxides can be considered to design novel support materials with enhanced properties. Along these lines, γ-Al$_2$O$_3$[25−27] and/or ZrO$_2$[28−30] are among the promising choices for the secondary oxides that can be used in combination with TiO$_2$ for improving the sulfur tolerance of the NSR catalysts by suppressing the sulfur adsorption and promoting the sulfur desorption from the surface. It was reported that using a mixture of TiO$_2$ and γ-Al$_2$O$_3$ as a support material minimized the amount of SO$_x$ deposit on a Pt/Ba/γ-Al$_2$O$_3$ catalyst and enhanced the NO$_x$ storage of the sulfur-exposed catalysts.[21] It was also suggested that the interface between Al$_2$O$_3$ and TiO$_2$ plays an important role in sulfate decomposition and desorption processes.[24]

Despite the established sulfur resisting effect of TiO$_2$ as an additive in the composition of the Pt/Ba/γ-Al$_2$O$_3$ NSR catalysts, most of the fundamental aspects regarding the influence of TiO$_2$ on the interaction between the NO$_x$ storage component and the support material have not yet been elucidated in detail. In addition, the effect of the TiO$_2$ on the surface distribution and the thermal stability of the catalytic species formed on the NO$_x$

* To whom correspondence should be addressed. E-mail: ozensoy@fen.bilkent.edu.tr.
† Bilkent University.
‡ Institute of Material Science and Nanotechnology.

Nature of the Ti−Ba Interactions

J. Phys. Chem. C, Vol. 113, No. 25, 2009 **11015**

storage systems as a function of the surface BaO loading have not been thoroughly investigated. In order to elucidate some of these crucial aspects, in the current study, we synthesized a TiO$_2$/γ-Al$_2$O$_3$ binary oxide support material via a sol−gel process and characterized its thermal structural changes using various analytic probes. Next, TiO$_2$/γ-Al$_2$O$_3$ binary oxide support material was further functionalized with different loadings of a Ba-containing NO$_x$ storage component in order to obtain a ternary oxide NO$_x$ storage material in the form of BaO/TiO$_2$/γ-Al$_2$O$_3$ (or Ba(NO$_3$)$_2$/TiO$_2$/γ-Al$_2$O$_3$). Thus, the primary focus of the current work is to examine the structure and thermal stability of the binary TiO$_2$/γ-Al$_2$O$_3$ oxide and to follow the surface and bulk transformations occurring on the BaO/TiO$_2$/γ-Al$_2$O$_3$ system at various temperatures, in order to shed light on the sulfur tolerance effect of TiO$_2$ in complex NSR systems.

2. Experimental Section

2.1. Sample Preparation. *Synthesis of TiO$_2$/γ-Al$_2$O$_3$ Support Material.* The binary TiO$_2$/γ-Al$_2$O$_3$ oxide with a relative TiO$_2$ molar ratio of TiO$_2$/(TiO$_2$ + Al$_2$O$_3$) = 0.31 was prepared via the sol−gel method, using a TiO$_2$ precursor and γ-Al$_2$O$_3$ as starting materials. In this synthetic protocol,[31] TiCl$_4$ (Fluka, titanium(IV) chloride solution ∼0.1 M in 20% hydrochloric acid) was used as a TiO$_2$ precursor. Precursor solution was added dropwise to a certain volume of precooled deionized water under continuous stirring so that the concentration of the precursor in the solution was adjusted to ∼1 M. In order to prevent the formation of Ti(OH)$_4$ explosively generated from the heat of the exothermic hydrolysis reaction, the temperature during the addition of the precursor was kept below 333 K by placing the solution beaker in an ice bath. After the complete dilution of the precursor solution with deionized water, γ-Al$_2$O$_3$ (PURAL-OX, 200 m^2/g, SASOL GmbH, Germany) was slowly added to the aqueous solution under constant stirring at room temperature. Next, the slurry was continuously stirred and 30 vol % NH$_3$ was slowly added to the solution in order to maintain a condition where pH ≥ 9.0. Gel formation started to be observed after the pH adjustment. The obtained white gel was aged for 24 h under ambient conditions and then filtered and washed with distilled water until the effluent was free of chloride ions confirmed by the AgNO$_3$ test. After that, the product was dried at 423 K for 2 h and ground into a fine powder form. Thermal evolution of the obtained support material was further investigated after various calcination steps (with durations of 2 h/step) in an Ar atmosphere at different temperatures (423−1273 K). Synthesized TiO$_2$/γ-Al$_2$O$_3$ binary oxide material is referred to as Ti/Al in the text.

Synthesis of BaO/TiO$_2$/γ-Al$_2$O$_3$ NO$_x$ Storage Materials. BaO/TiO$_2$/γ-Al$_2$O$_3$ samples with different Ba loadings (8 and 20 wt % BaO) were synthesized by conventional incipient wetness impregnation of the TiO$_2$/γ-Al$_2$O$_3$ binary oxide support material. In this synthetic protocol, the support material was impregnated with an aqueous solution of barium nitrate (ACS Reagent, ≥99% purity, Riedel-de Haën). Thus, the state of the freshly prepared samples can be viewed as model systems which mimic the NO$_x$-loaded or nitrate-saturated storage materials. After impregnation, synthesized Ba(NO$_3$)$_2$/TiO$_2$/γ-Al$_2$O$_3$ samples were dried at 353 K. Hence, presumably most of the nitrate ions originally present in the impregnation solutions with well-known concentrations of Ba(NO$_3$)$_2$ (aq) were deposited on the surface of the storage materials after the mild evaporation of the solvent at 353 K. Next, samples were calcined in Ar atmosphere for 2 h at different temperatures within 423−1273 K to obtain nitrate-free storage material. Such a thermal treatment series reveals an opportunity to study the thermal decomposition of nitrates,

although it should be noted that the decomposition characteristics of these nitrates originating from liquid precursors may differ from the nitrates which are stored via gas-phase NO$_x$ adsorption. After each temperature treatment, representative samples from the treated batches were collected for ex-situ analysis.

Compositions of the NO$_x$ storage materials and their acronyms used in the current text are as follows: 8Ba/Ti/Al and 20Ba/Ti/Al samples contained 8 and 20 wt % BaO, respectively, with balancing amounts of the TiO$_2$/γ-Al$_2$O$_3$ support material.

2.2. Experimental Methods. The specific surface areas (S_{BET}, m^2/g) of the samples were measured by a single-point Brunauer−Emmett−Teller (BET) method[32] via low-temperature isothermal adsorption−desorption of N$_2$. The sample was degassed under vacuum at room temperature for 1 h, prior to adsorption measurements in order to outgas the physisorbed moisture. The measurements were performed using a Micromeritics ASAP 2000 gas sorption and porosimetry system.

The powder XRD patterns were recorded using a Rigaku diffractometer, equipped with a Miniflex goniometer and an X-ray source with Cu Kα radiation, at λ = 1.5418 Å, 30 kV, and 15 mA. The powder samples were pressed and affixed to standard-sized glass slides and scanned in the 10−80°, 2θ range with a scan rate of 0.01 deg s^{-1}. Diffraction patterns were assigned using Joint Committee on Powder Diffraction Standards (JCPDS) cards supplied by the International Centre for Diffraction Database (ICDD).

The Raman spectra were recorded on a HORIBA Jobin Yvon LabRam HR 800 instrument, equipped with a confocal Raman BX41 microscope, spectrograph with an 800 mm focal length, and a CCD detector. The Raman spectrometer was equipped with a Nd:YAG laser (λ = 532.1 nm). During the Raman experiments, the laser power was tuned to 20 mW, measured at the sample position, in order to minimize the sample heating effects. Before the Raman measurements, the powder samples were mechanically dispersed onto a single-crystal Si holder. The incident light source was dispersed by holographic grating with a 600 grooves/mm and focused onto the sample by using a 50× objective. The confocal hole and slit entrance were set at 1100 and 200 μm, respectively. The spectrometer was regularly calibrated by adjusting the zero-order position of the grating and comparing the measured Si Raman band frequency with the typical reference value of 520.7 cm^{-1}. All Raman spectra were acquired within 100−4000 cm^{-1} with an acquisition time of 213 s and a spectral resolution of 4 cm^{-1}. Bulk anatase (TiO$_2$, anatase-nano powder, Inframat Advanced Materials·, purity ≥ 99.9%) and rutile (obtained after calcination of the aforementioned anatase sample at 1273 K for 2 h) polymorphs of TiO$_2$ and bulk Ba(NO$_3$)$_2$ (ACS Reagent, ≥99% purity, Riedel-de Haën) were used for the reference Raman spectra.

The surface acidity of the studied oxide systems was investigated by in-situ Fourier transform infrared (FTIR) spectroscopy measurements of chemisorbed pyridine. Pyridine (Merck KGaA, purity > 99.0%) was used as a basic probe molecule in this procedure and further purified via several freeze−thaw−pump cycles before adsorption. FTIR spectroscopic measurements were carried out in transmission mode in a batch-type catalytic reactor. FTIR spectra were recorded using a Bruker Tensor 27 FTIR spectrometer and a Hg−Cd−Te (MCT) detector (cooled with liquid nitrogen), where each spectrum was acquired by averaging 128 scans with a spectral resolution of 4 cm^{-1}. The samples were mounted into the IR cell, consisting of a five-way stainless steel cube equipped with optically-polished BaF$_2$ windows. This IR cell was connected to a gas manifold (including a dual-stage rotary vane pump and

turbomolecular pumps) so that the pressure in the cell could be varied within $1000-10^{-6}$ Torr. About 20 mg of finely ground powder sample was pressed onto a high-transmittance, lithographically etched fine-tungsten mesh which was mounted on a gold-coated copper sample holder assembly, attached to a ceramic vacuum feedthrough. A K-type thermocouple was spot welded to the surface of a thin tantalum plate attached on the W grid to monitor the sample temperature. After the sample was mounted in the IR cell, it was gradually heated to 373 K in vacuum and kept at that temperature overnight (about 12 h before the experiments) in order to ensure the removal of water from the surface. In an attempt to minimize the effect of background water (i.e., readsorption from the walls of the IR cell and the gas manifold), the system was frequently baked out.

Prior to each pyridine adsorption experiment, the sample surface was activated (dehydrated) in the IR cell by ramping the sample temperature to 623 K and subsequently outgassing the sample at the same temperature for 1 h under vacuum (residual pressure $< 10^{-4}$ Torr). After this pretreatment protocol, the sample was cooled down to 323 K and a background spectrum of the clean, adsorbate-free sample was obtained (with a residual reactor pressure $< 1 \times 10^{-5}$ Torr). Then, the sample was exposed to a precisely controlled dose of pyridine vapor ($P_{pyridine} = 3.0$ Torr) for 15 min at 323 K. After the saturation of the sample surface (15 min), the system was evacuated at room temperature ($P_{reactor} < 1 \times 10^{-4}$ Torr). After the acquisition of the pyridine-saturated sample spectrum at 323 K, the sample was heated in vacuum to various temperatures within $323-723$ K and then cooled back to 323 K for the sample spectra acquisition.

The morphology, elemental composition, and dispersion of the deposited Ba and Ti species on the surface of the samples were investigated using a scanning electron (SE) microscope, equipped with an EDX spectrometer. SEM and EDX data were acquired using a Zeiss EVO40 environmental SEM that is equipped with a LaB_6 electron gun, a vacuum SE detector, an elevated pressure SE detector, a backscattering electron detector (BSD), and a Bruker AXS XFlash 4010 detector. Samples for SEM and EDX analysis were prepared by grinding the powder samples into fine particles and mechanically dispersing them on an electrically conductive carbon film which was placed on an aluminum sample holder. No additional coatings or dispersive liquids were used for the SEM and EDX sample preparation. SEM images were obtained using a vacuum SE detector where electron acceleration voltage of the incident beam was varied within $10-20$ kV and the samples were kept typically at $\leq 5 \times 10^{-5}$ Torr inside the SEM. All of the EDX data were collected using an electron acceleration voltage of 20 kV and a working distance of 15 mm. For all of the EDX elemental mapping studies, at least four independent areas of identical dimensions on the same catalyst sample were investigated in order to ensure the reproducibility of the results.

3. Results and Discussion

3.1. Thermal Evolution of the TiO_2/γ-Al_2O_3 Binary Oxide Support Material. *3.1.1. Specific Surface Area Measurements.* Thermal changes in the textural properties of the sol−gel-synthesized TiO_2/γ-Al_2O_3 system and the influence of the presence of a NO_x storage component on the support surface were examined by specific surface area measurements. Figure 1 illustrates the temperature dependence of the S_{BET} (m^2/g) of the Ti/Al support material and the 20Ba/Ti/Al sample within $623-1273$ K.

It is seen in Figure 1 that the specific surface areas corresponding to both samples are strongly affected by the
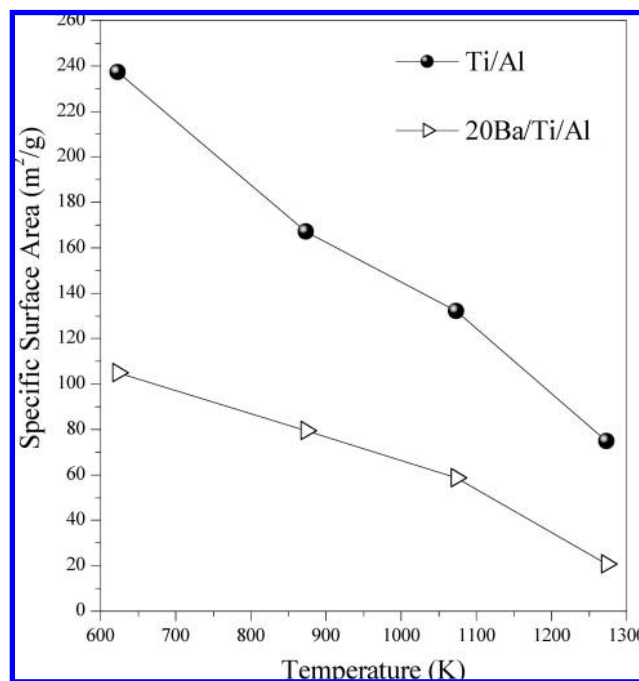

Figure 1. Specific surface area data for Ti/Al and 20Ba/Ti/Al samples after thermal treatments at various temperatures (see text for details).

thermal treatments, and S_{BET} values tend to decrease in a monotonic fashion with increasing temperature. Such a behavior is rather typical for thermal processes leading to sintering and/or phase transformations. When the S_{BET} values of Ti/Al samples are compared with that of the Ba/Ti/Al sample, it is readily observed that introduction of the Ba-containing NO_x storage component lowers the S_{BET} by partially blocking the pore structure of the support material. A similar behavior was also observed when thermal changes of the S_{BET} for Al_2O_3 was compared with that of the $Ba(NO_3)_2/Al_2O_3$ samples where the presence of the Ba component decreases the surface area of the Al_2O_3 support material (data not shown).

For the temperature interval within $623-1073$ K, monotonic attenuation of the specific surface area values of the Ti/Al sample can be attributed to the growth of the anatase and γ-Al_2O_3 crystallite sizes since XRD data presented in section 3.1.2 does not reveal any significant polymorphic changes in neither anatase nor γ-Al_2O_3 phases. It was reported in the literature[33] that anatase has a greater sintering rate than γ-Al_2O_3 due to its larger specific surface energy and lower activation energy for surface diffusion. Thus, the thermally induced attenuation of the surface area of the Ti/Al sample is likely to be predominantly associated with the Ti-containing component.

XRD data presented in section 3.1.2 also indicate that the large decrease in the specific surface area of the support Ti/Al material after calcination at 1273 K can be ascribed to the transformation of the anatase phase into rutile and a partial transformation of the γ-Al_2O_3 phase into corundum (i.e., α-Al_2O_3). On the other hand, the significantly lower S_{BET} values corresponding to the 20Ba/Ti/Al NO_x storage system within $1073-1273$ K is probably due to sintering and the formation of solid solutions between the oxide components present in the system. These arguments are further discussed in light of the XRD, Raman, and EDX data presented in the sections below.

3.1.2. XRD and Raman Studies on the TiO_2/γ-Al_2O_3 Support Material. The XRD data presented in Figure 2 reveal the thermal behavior of the Ti/Al system within $300-1273$ K. The

Nature of the Ti—Ba Interactions

J. Phys. Chem. C, Vol. 113, No. 25, 2009 **11017**

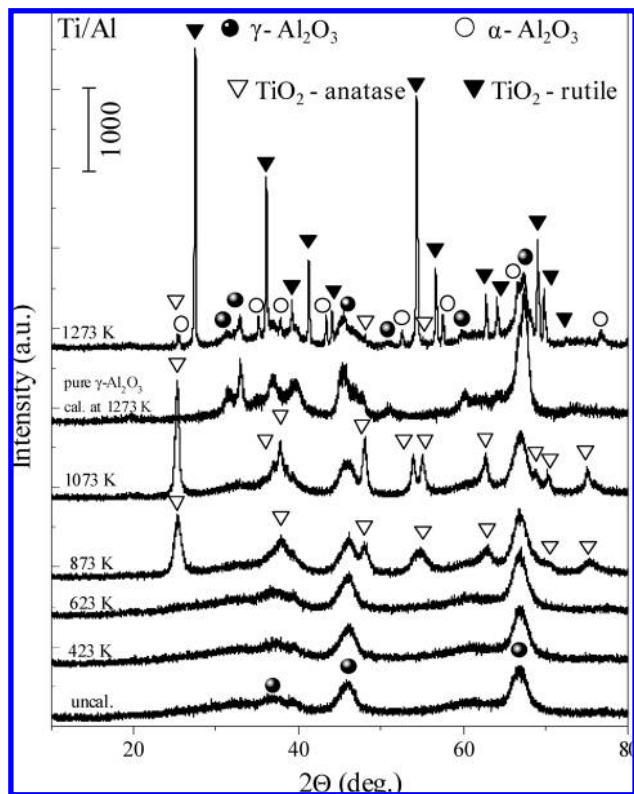**Figure 2.** XRD patterns of the Ti/Al samples before and after calcination in the temperature range of 423−1273 K. The XRD profile of pure γ-Al_2O_3 calcined at 1273 K is also shown in the figure.

XRD profile of pure γ-Al_2O_3 calcined at 1273 K is also shown in the same figure. Only very broad diffraction features associated with the γ-Al_2O_3 (JCPDS 29-0063, marked with ●) were detected in the XRD patterns of the uncalcined and calcined Ti/Al samples at 423 and 623 K. As can be seen in Figure 2, no discernible diffraction peaks due to other crystalline phases can be observed at $T \leq 623$ K, suggesting that TiO_2 species present in the composite Ti/Al structure have a very small average crystallite size or are still in an amorphous form.

When the Ti/Al sample is thermally treated at 873 K, the diffraction peaks corresponding to the presence of anatase polymorph of TiO_2 become apparent (JCPDS 21-1272, marked with ▽), implying that some of the amorphous TiO_2 domains transform into anatase phase. Moreover, anatase crystallinity accentuated when the calcination temperature was increased to 1073 K. A significant change in the XRD pattern of the Ti/Al system took place after heat treatment at 1273 K. It is seen in Figure 2 that at 1273 K diffraction peaks corresponding to anatase start to attenuate in a significant manner. This observation is concomitant with the appearance of a new set of intense features associated with the rutile polymorph of TiO_2 (JCPDS 10-0173, marked with ▼). The XRD profile at this temperature also includes minor diffraction signals associated with the presence of α-Al_2O_3 (corundum, JCPDS 10-0173, marked with ○). These observations can be explained by considering a partial phase transformation from γ-Al_2O_3 to α-Al_2O_3 phases and a simultaneous increase in the crystallite sizes of the remaining γ-Al_2O_3 domains. This observation is also consistent with a former study[34] focusing on the effect of the presence of alumina on the titania phase transformations, suggesting that the anatase to rutile transformation is observed concomitantly with the formation of the corundum phase. It was also reported that alumina might be incorporated into the anatase lattice to form

a solid solution. Thus, at high temperatures where the anatase to rutile transformation starts to occur, α-Al_2O_3 can be directly formed from the aforementioned solution.

The anatase and rutile polymorphs of TiO_2 can also be sensitively identified by Raman spectroscopy. Raman spectra of the Ti/Al system before and after temperature treatments within 423−1273 K are presented in Figure 3. In addition, insets (i) and (ii) of Figure 3 show the reference Raman spectra and XRD patterns corresponding to bulk anatase and rutile. According to the factor group analysis,[35,36] anatase crystallizes in a tetragonal structure and belongs to the D_{4h}^{19} space group. The reference Raman spectrum of anatase (uppermost spectrum in the inset of Figure 3) consists of six Raman active modes ($1A_{1g}$, $2B_{1g}$, and $3E_g$) with positions at 144 (E_g), 197 (E_g), 399 (B_{1g}), 516 ($A_{1g} + B_{1g}$), 639 (E_g), and 796 cm^{-1} (E_g). The room-temperature Raman band at 516 cm^{-1} is split into two peaks centered at 513 (A_{1g}) and 519 cm^{-1} (B_{1g}).[37] Similarly, rutile also has a tetragonal structure;[38] however, it belongs to the D_{4h}^{14} space group and is characterized by a Raman spectrum with four Raman active modes ($A_{1g} + B_{1g} + B_{2g} + E_g$) and a two-phonon scattering band at 236 cm^{-1}. These four modes are visible in the rutile spectrum presented in the inset of Figure 3 at 143 (B_{1g}), 447 (E_g), 612 (A_{1g}), and 826 cm^{-1} (B_{2g}). Furthermore, it is worth emphasizing that the rutile band at 143 cm^{-1} has a very similar frequency to the E_g band of anatase at 144 cm^{-1}. However, it should be noted that the intensity of the E_g band of anatase is significantly more pronounced than that of the B_{1g} band of rutile.

Raman spectra of the Ti/Al samples of the uncalcined and calcined samples at 423 and 623 K consist of broad and relatively weak bands at around 170, 418, and 630 cm^{-1} as well as a complex set of features within 800−900 cm^{-1}. Comparison of these features with the reference (bulk) anatase spectrum in the inset (i) of Figure 3 reveals that these features can be attributed mostly to anatase. The presence of broad and low-intensity anatase features in the Ti/Al Raman spectra corresponding to the thermal window within 300−623 K indicates that anatase phase exhibits complex structure with a poor crystallinity, consistent with the XRD data given in Figure 2. After thermal treatments above 873 K, anatase features become much more pronounced and shift to lower frequencies with a considerable decrease in their full-width at half-maximum (fwhm) values. It is well known that the crystallite size has a profound influence on the nature of the Raman features originating from powder samples.[39] Spectral broadening and the frequency shifts of the Raman bands corresponding to TiO_2 nanocrystals have been previously reported by several authors in the literature.[40,41] These spectral changes were mainly attributed to phonon confinement, oxygen deficiencies (formation of nonstoichiometric phases), and pressure effects on the grains, induced by the surrounding grains or by the surface tension. It was suggested that if the influence of the surface defects is neglected, nanocrystallite anatase Raman features shift to lower frequencies with respect to their bulk values and their fwhm values decrease as the crystallite size increases. However, as reported in the literature,[42] the fwhm values are more sensitive to the crystallite size changes while the Raman frequencies are relatively less influenced by similar changes. Therefore, it is conceivable that the observed decrease in the fwhm values of the Raman features of the Ti/Al system can be related to the growth and ordering of the anatase phase above 623 K. This result is also in good agreement with the XRD data presented in Figure 2. A similar trend also holds for the Raman spectra corresponding to 873 and 1073 K.
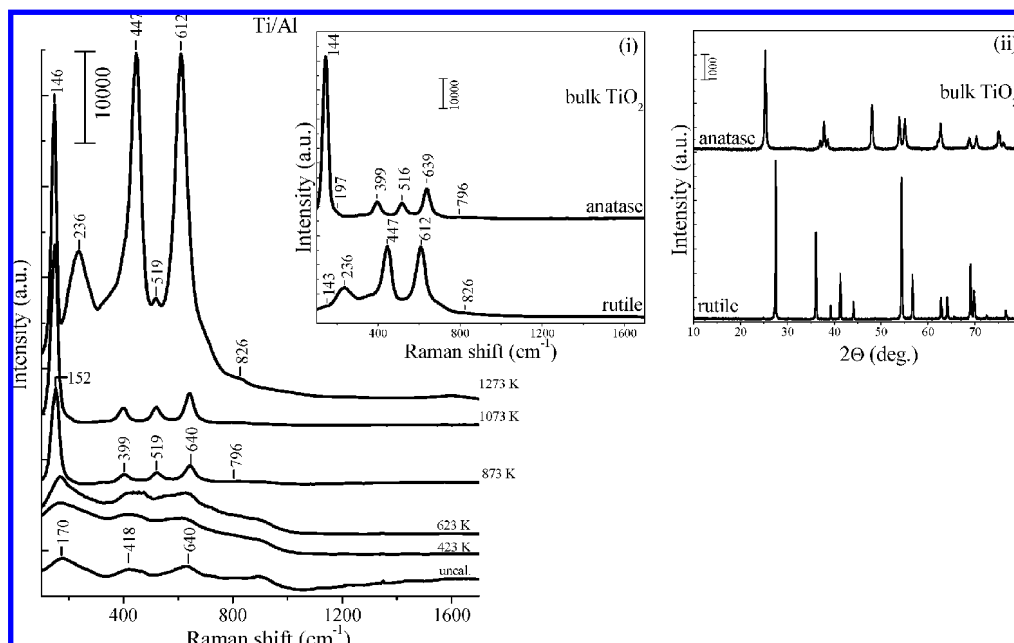
Figure 3. Temperature-dependent ex-situ Raman spectra corresponding to the calcined (423−1273 K) and uncalcined Ti/Al samples. Insets (i) and (ii) present the Raman and XRD data for the bulk anatase and rutile reference materials, respectively.

It is evident from the topmost spectrum in Figure 3 that a further increase in the calcination temperature to 1273 K results in an incomplete phase transformation from the anatase to the rutile phase. The prominent Raman bands at 236, 447, 612, and 826 cm^{-1} in the topmost spectrum can readily be assigned to the rutile structure. However, the presence of an intensive Raman band at 146 cm^{-1} and the weakly expressed feature at 519 cm^{-1} in the topmost spectrum in Figure 3 signify the coexistence of the anatase and rutile phases in the Ti/Al system. It is worth mentioning that the reference Raman spectrum of rutile (inset (i) of Figure 3) was obtained after thermal treatment of pure anatase at 1273 K for 2 h. Thus, it is very likely that the bottommost spectrum in the inset (i) of Figure 3 almost exclusively originates from the rutile phase. This is also evident in the XRD data for the same reference sample presenting sharp features associated with the rutile phase given in the inset (ii) of Figure 3. This is not surprising since previous studies[43] reveal that a complete anatase to rutile phase transformation was reported on bulk TiO_2 samples at temperatures as low as 873 K. Observation of the anatase to rutile phase transformation on the Ti/Al surface at a higher temperature with respect to the pure TiO_2 system suggests the stabilization of the anatase phase on the Ti/Al surface due to a strong interaction between the TiO_2 and γ-Al_2O_3 domains. The influence of Al_2O_3 on the phase transformation of TiO_2 nanoparticles and the structure of the composite was reported in a former study by differential scanning calorimetric (DSC) and XRD analysis.[44] It was found that the bonding interactions between the $[TiO_6]$ octahedra on the anatase surface and the $[AlO_6]$ octahedra result in a retardation of the anatase to rutile phase transition and impedes the growth of nanometer-sized TiO_2 domains. In other words, strong interaction between the anatase and γ-Al_2O_3 domains (where packing of the oxide ions possess cubic symmetry in both structures) leads to the formation of a solid solution which, in turn, hinders the anatase to rutile transition by increasing the corresponding phase transformation temperature. On the other hand, at high enough temperatures where the anatase domains in the solution start to transform into the hexagonal rutile structure, rutile and γ-Al_2O_3 domains

begin to phase segregate. This is due to the relatively low solubility of the hexagonal rutile structure in the cubic γ-Al_2O_3 lattice.[34] Thus, after this phase segregation, small γ-Al_2O_3 crystallites leaving the solution can readily undergo a phase transition and form the α-Al_2O_3 structure at temperatures that are significantly lower than that of the bulk γ-Al_2O_3 system.

3.2. Thermal Evolution of the Ba/Ti/Al Ternary Oxide NO$_x$ Storage Material. *3.2.1. XRD and Raman Studies on the Ba/Ti/Al System.* Figure 4a and 4b shows the XRD patterns of the uncalcined and calcined 8Ba/Ti/Al and 20Ba/Ti/Al samples. The diffraction peaks corresponding to γ-Al_2O_3 (●) and crystalline $Ba(NO_3)_2$ (JCPDS 24-0053, marked with ★) were detected in both samples, before and after calcination at 423 and 623 K. As expected, $Ba(NO_3)_2$ species for the 20Ba/Ti/Al sample are characterized with considerably higher crystallinity than that of the samples with the lower Ba content. However, an increase in the calcination temperature to 873 K leads to the complete disappearance of the $Ba(NO_3)_2$-related peaks in the diffraction patterns of both samples independent of the Ba content.

The thermal treatment at higher temperatures results in significant alterations in the crystallographic composition of the Ba/Ti/Al samples with different Ba contents. Only the broad diffraction features associated with the γ-alumina and minor features related to anatase formation (marked with ▽) are visible in the XRD profile of the 8Ba/Ti/Al sample calcined at 873 K given in Figure 4. On the other hand, at the same calcination temperature, 20Ba/Ti/Al sample reveals γ-Al_2O_3 features, coexisting with strong signals associated with the $BaTiO_3$ structure having a cubic *Pm3m* symmetry (JCPDS 74-1964, marked with ▼). With increasing the calcination temperature up to 1273 K, this phase undergoes a further structural reconfiguration due to its interaction with the anatase and Al_2O_3 domains present in the system. This is also evident from the attenuation of the anatase and $BaTiO_3$ peak intensities at 1273 K and the formation of a new set of doublets separated by ~0.4°. This new set of features is tentatively assigned to the formation

Nature of the Ti−Ba Interactions

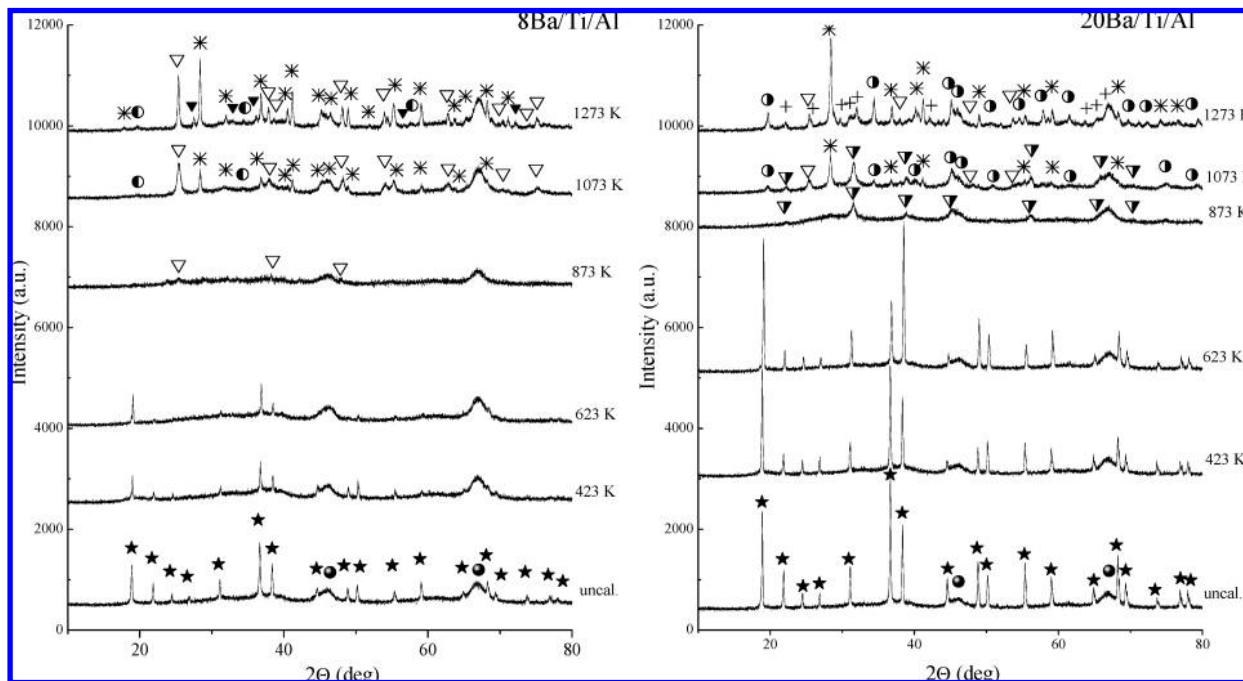*J. Phys. Chem. C, Vol. 113, No. 25, 2009* **11019**

Figure 4. Thermal behavior of the XRD profiles corresponding to the calcined (423−1273 K) and uncalcined Ba/Ti/Al ternary oxide NO$_x$ storage materials with different BaO loadings: (a) 8Ba/Ti/Al and (b) 20Ba/Ti/Al.

of BaTi$_2$O$_5$ and/or a new composite phase in the form of Ba$_x$Ti$_y$O$_z$ or Ba$_x$Ti$_y$Al$_z$O$_n$ (marked with the symbol + in Figure 4).

It is also visible in Figure 4a and 4b that after the thermal treatments at 1073 and 1273 K, relatively sharp diffraction features attributed to the presence of anatase and a complex phase in the form of Ba$_{1.23}$Al$_{2.46}$Ti$_{5.54}$O$_{16}$ (JCPDS 033-0133, marked with an asterisk (*)) appear in the XRD patterns of 8Ba/Ti/Al and 20Ba/Ti/Al samples. Degree of crystallinity of the complex oxide increases with increasing the calcination temperature from 1073 to 1273 K. However, the intensity ratios between these two phases are dissimilar for the two samples with different Ba contents. As can be seen in Figure 4, within 1073−1273 K, the anatase-related diffraction features originating from the 20Ba/Ti/Al sample show considerably lower intensities in comparison with those observed for the 8Ba/Ti/Al sample. In addition to these observations, within 1073−1273 K, rather weak and broad features (marked with marked with ◖) are also detected in Figure 4a and 4b. These minor features are assigned to the presence of BaAl$_2$O$_4$ (JCPDS 17-0306). BaAl$_2$O$_4$ signals are characterized with considerably higher intensities for the 20Ba/Ti/Al sample with the higher Ba content. It is worth mentioning that the increase in calcination temperature to 1273 K for the 8Ba/Ti/Al sample (Figure 4a) is accompanied by a phase transformation from anatase to rutile. However, rutile formation is not observed for the 20Ba/Ti/Al sample at 1273 K.

Comparison of the temperature-dependent XRD profiles of the Ti/Al (Figure 2) and Ba/Ti/Al systems (Figure 4) at 1273 K reveals that anatase to rutile polymorphic phase transformation is suppressed in the presence of Ba, particularly for high Ba loadings. This can probably be ascribed to the increased interaction between the Ba and Ti domains and solid-state reactions leading to a structural reconfiguration and formation of a solid solution between the components. A similar interaction where the formation of a solid solution in the form of Ba(Ti$_{1−2x}$Al$_{2x}$)O$_{3−x}$ was also reported in a former study[45] where the inhibition of the grain growth in BaTiO$_3$ by addition of Al$_2$O$_3$ was investigated.

Figure 5a and 5b displays the temperature-dependent ex-situ Raman spectra corresponding to the uncalcined and calcined (423−1273 K) 8Ba/Ti/Al and 20Ba/Ti/Al samples. Raman spectra corresponding to Ba(NO$_3$)$_2$, BaO, Ba(NO$_3$)$_2$/γ-Al$_2$O$_3$, and BaO/γ-Al$_2$O$_3$ were discussed in detail in one of our recent studies.[46] On the basis of our previous studies as well as others in the literature,[46−50] it is clear that Raman spectra before calcination and after calcination at 423 and 623 K predominantly consist of Raman bands, which can readily be assigned to crystalline Ba(NO$_3$)$_2$. The most dominant band at 1044 cm$^{−1}$ is attributed to the symmetric stretching mode of the nitrate (NO$^−_3$) ion, the band with medium intensity at 728 cm$^{−1}$ is due to the nitrate bending mode, and the group of weak bands at 1634, 1357, and 1406 cm$^{−1}$ are assigned to the longitudinal optical (LO) and transverse optical (TO) modes of the antisymmetric stretch, respectively. The observed lattice phonon band at 134 cm$^{−1}$ is also an indicator for the high degree of crystallinity of the Ba(NO$_3$)$_2$ domains.[46,47] In addition to these bands, very weakly expressed features at around 399 and 639 cm$^{−1}$ and a broad shoulder in the spectral range of 800−900 cm$^{−1}$ can be also seen. These broad and minor features are related to similar but sharper features observed in the anatase reference spectrum (inset (i) of Figure 3) and point to the presence of TiO$_2$ in a relatively disordered form. However, due to the poorly defined nature of these signals, the presence of amorphous TiO$_2$ domains cannot be ruled out in the Raman data given in Figure 5. It should also be noted that such amorphous TiO$_2$ domains are also elusive to detect in the XRD measurements.

In accordance with the XRD data given in Figure 4, an increase in the calcination temperature to 873 K results in the complete disappearance of all of the nitrate-related Raman bands in Figure 5. This is particularly evident by considering the vanishing bands at this temperature such as the Ba(NO$_3$)$_2$ lattice phonon band (134 cm$^{−1}$) and the symmetric nitrate stretching mode (1044 cm$^{−1}$). The Raman spectra in Figure 5a and 5b at 873 K are characterized by relatively weak bands at 399, 516, and 639 cm$^{−1}$, a shoulder at 796 cm$^{−1}$, and a stronger band at 144 cm$^{−1}$ that can be assigned to anatase. This result is also in a good agreement with the XRD data (Figure 4) and is indicative
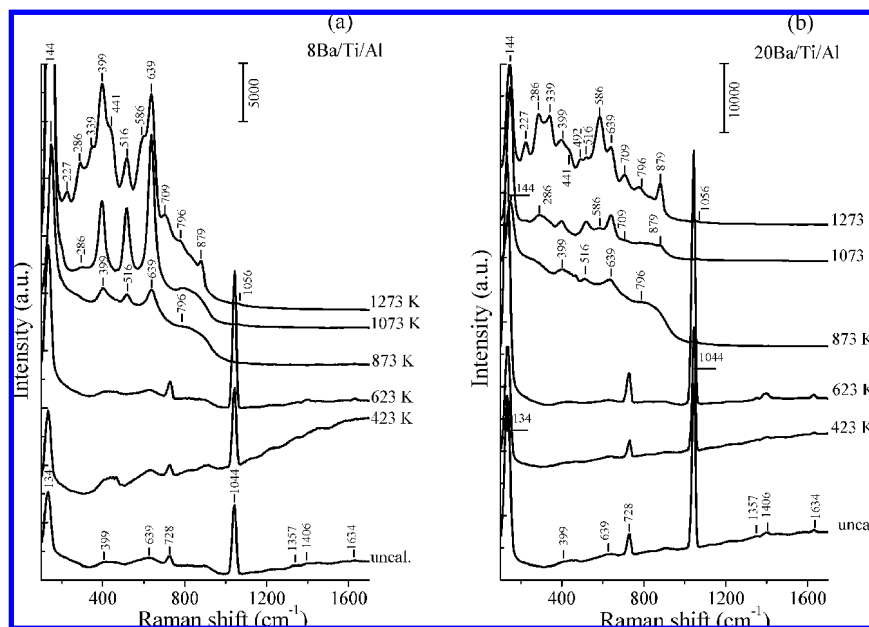
Figure 5. Temperature-dependent ex-situ Raman spectra corresponding to the calcined (423−1273 K) and uncalcined Ba/Ti/Al samples with different Ba loadings: (a) 8Ba/Ti/Al and (b) 20Ba/Ti/Al.

for the full thermal decomposition of the $Ba(NO_3)_2$ to amorphous BaO under these conditions. Decomposition of $Ba(NO_3)_2$ may also be facilitated by the formation of complex Ba−Ti mixed oxides such as $BaTiO_3$, $Ba_{1.23}Al_{2.46}Ti_{5.54}O_{16}$, as well as other mixed oxides mentioned above whose formation triggers the depletion of BaO sites that are generated upon decomposition of $Ba(NO_3)_2$. The first-order Raman scattering is symmetry forbidden for crystalline BaO;[47,51] however, the defect-rich BaO structure is characterized by a broad set of weak bands within the spectral region of 350−500 cm^{-1}.[46,47] Therefore, in Figure 5a and 5b, Raman spectra corresponding to temperatures higher than 623 K may contain the weak BaO signal that is likely to be convoluted with the stronger anatase features within 350−500 cm^{-1}.

Further elevated temperature treatments of the Ba/Ti/Al samples at 1073 and 1273 K lead to noticeable spectral Raman changes for the Ti/Ba/Al samples with dissimilar Ba loadings. It is visible in Figure 5 that at 1073 K, 8Ba/Ti/Al sample is characterized by more intensive anatase Raman bands compared to the 20Ba/Ti/Al system. Figure 5b shows that the Raman spectrum corresponding to the 20Ba/Ti/Al sample at 1073 K contains additional Raman bands at 286, 586, 709, and 879 cm^{-1} other than the anatase. The intensities of these additional features increase with increasing calcination temperature to 1273 K and become much more pronounced in comparison with the anatase-related bands. These features can also be seen in Figure 5a at 1273 K, although in this case the intensities of these additional features are smaller and the anatase-related Raman bands dominate. When these observations are considered in light of the crystallographic changes detected in the XRD experiments presented in Figure 4, which reveal an increase in the relative anatase to $Ba_{1.23}Al_{2.46}Ti_{5.54}O_{16}$ intensity ratios when the temperature is increased from 1073 to 1273 K, it can be argued that these additional Raman features observed in Figure 5 can be associated with the $Ba_{1.23}Al_{2.46}Ti_{5.54}O_{16}$ phase. It should also be mentioned that due to the complex nature of these high-temperature Raman features revealing a convoluted set of bands, contributions coming from other Ba−Ti−Al mixed oxide species cannot be ruled out either.

In previous studies,[52−55] it was found that the crystallinity and thermal stability of the Ba nitrates on pure γ-Al_2O_3 surface strongly depend on the Ba loading and the interaction of the storage phase with the γ-alumina support material. Evidence for the presence of two different types of nitrate species with different thermal stabilities (surface nitrates that are associated with a monolayer BaO on the alumina support and a bulk-like nitrate species that forms on this thin BaO layer) on the $NO_2(g)$-saturated BaO/γ-Al_2O_3 sample has been reported.[53] The results concerning the thermal stability of the formed species in these investigations are also in good agreement with our previous study[46] on BaO/γ-Al_2O_3 samples saturated with nitrates from solution precursors where the Raman data indicated that the formed nitrates on the surface of the Ba/Al sample containing 20 wt % BaO decompose at a considerably higher temperature than that of the 8Ba/Al sample. Raman spectra[46] acquired after thermal treatments at 623, 873, and 1073 K revealed that the nitrate decomposition was completed at 873 K for the 8Ba/Al sample, whereas nitrate signal was still visible at 873 K for the 20Ba/Al sample and vanishes at 1073 K. Thus, the complete thermal decomposition of nitrates on 8Ba/Al saturated with nitrates from solution precursors occurs at a temperature which is about 250 K lower than that of the 20Ba/Al sample.[46]

In the current synthetic procedure, the mixed Ba/Ti/Al ternary oxide NO_x storage systems have the same BaO to support weight ratio as that of the Ba/Al binary oxide NO_x storage materials that were previously investigated.[46] However, the current results demonstrate that on the Ba/Ti/Al ternary oxide NO_x storage system, nitrate species are completely decomposed at 873 K regardless of the loading of the Ba-containing component. The presence of TiO_2 mainly in the form of anatase on the 20Ba/Ti/Al sample results in a decrease in the thermal stability of the nitrate species on the surface, which is closely similar to that of the 8Ba/Ti/Al sample. This result indicates that the presence of TiO_2 domains actively influences the nitrate decomposition temperature by modifying the interaction between the NO_x storage units and its underlying support material. In the Ba/Ti/Al ternary system, it is apparent that the TiO_2 domains show a high affinity toward $Ba(NO_3)_2$ and BaO domains. Thus,

Nature of the Ti−Ba Interactions
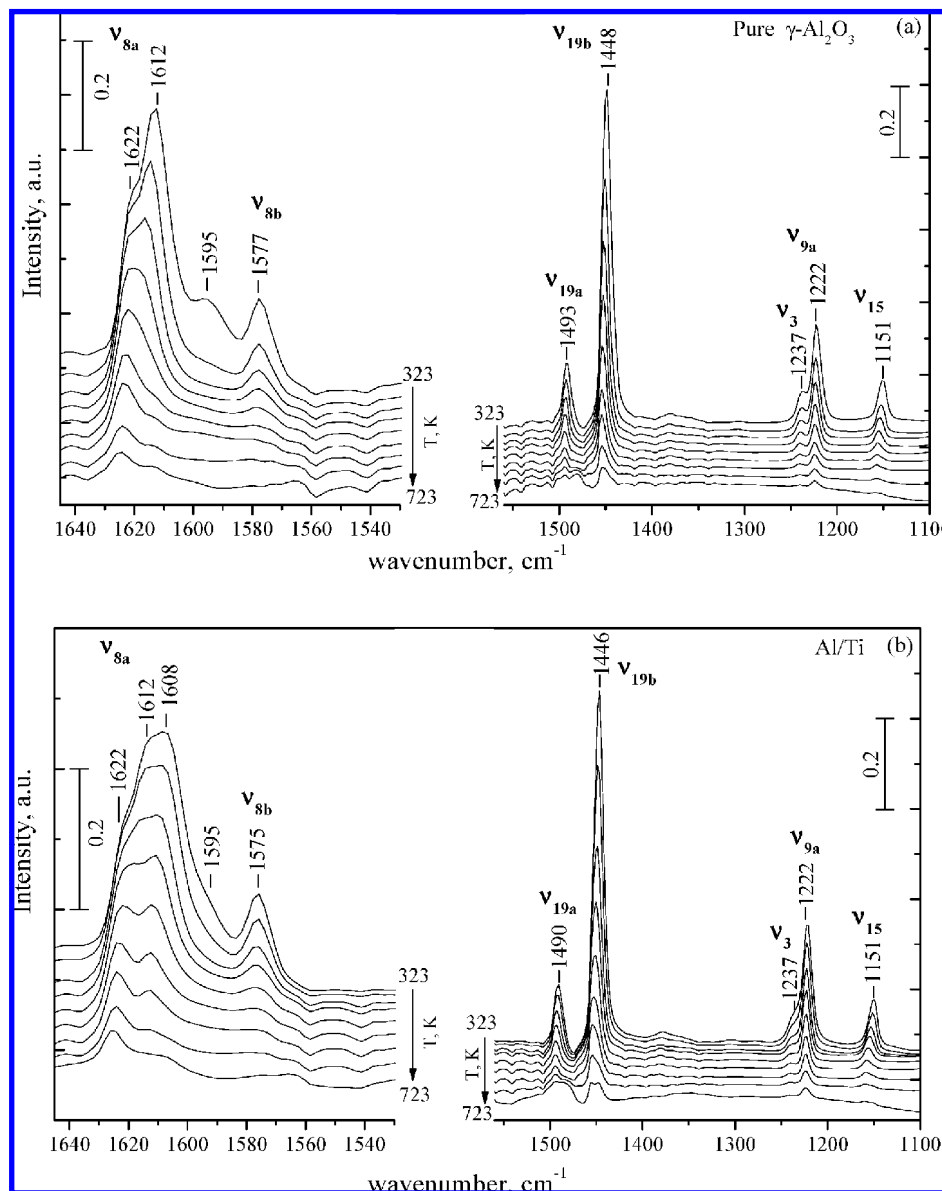
J. Phys. Chem. C, Vol. 113, No. 25, 2009 **11021**

Figure 6. Temperature-dependent (323−723 K) FTIR spectra for chemisorbed pyridine species formed at room temperature on the surface of pure γ-Al$_2$O$_3$ (a) and on the binary mixed oxide TiO$_2$/γ-Al$_2$O$_3$ system precalcined at 873 K (b).

it is conceivable that during the introduction of the Ba domains on the Ti/Al system via impregnation Ba domains prefer to anchor predominantly on the TiO$_2$ islands. This argument is also consistent with the SEM/EDX results presented below. Such a preferential interaction between Ti- and Ba-containing domains may influence the surface dispersion and morphology of NO$_x$ storage units resulting in a dissimilar thermal stability compared to the simpler Ba/Al system.

Furthermore, it is also well known that the amount of adsorbed species and their thermal stabilities on oxide surfaces are closely related to the surface acidity of the solid material, i.e., the presence of surface protons associated with the Brönsted acidity or coordinatively unsaturated cationic centers associated with the Lewis acidity.[56] The surface acidity of the composite TiO$_2$/γ-Al$_2$O$_3$ oxide was previously investigated in a former study[57] by Fourier transform infrared spectroscopy (FTIR). It was found that TiO$_2$ in this mixed oxide is characterized by high Lewis surface acidity due to the formation of small TiO$_2$ crystallites on the surface of the alumina particles. This could also be one of the key parameters associated with the consider-

ably lowered thermal stability of the stored nitrates in the Ba/Ti/Al system in comparison with that of the BaO/γ-Al$_2$O$_3$ system.

Along these lines, FTIR experiments were also performed, in which chemisorbed pyridine was used as a probe molecule in order to examine the nature and strength of the surface acid sites present on the currently investigated oxide materials (i.e., γ-Al$_2$O$_3$, γ-Al$_2$O$_3$−TiO$_2$, 8(20)Ba/γ-Al$_2$O$_3$, and 8(20)Ba/γ-Al$_2$O$_3$−TiO$_2$).

***3.2.2. Surface Acidity: FTIR Spectra of Chemisorbed Pyridine.* 3.3.2.1. Adsorbed Pyridine on Pure γ-Al$_2$O$_3$ and on the Binary Mixed Oxide TiO$_2$/γ-Al$_2$O$_3$ System.** As described in the Experimental Section, the surfaces of the γ-alumina and Ti/Al support materials were both calcined at 873 K in Ar(g) prior to the chemisorption experiments, followed by in-situ activation/evacuation at 623 K for 1 h. After the activation protocol, the samples were exposed to pyridine vapor (3 Torr) at 323 K for 15 min. Then this was followed by an evacuation step at 323 K and subsequent annealing steps at various temperatures within 373−723 K. Figure 6 presents the evolution

of the relevant pyridine vibrational bands as a function of the annealing temperatures. These vibrational modes within $1640-1100$ cm^{-1} correspond to various pyridine ring stretching modes (v(C−N) and v(C−C)). Room-temperature pyridine adsorption on both surfaces reveals bands located at 1151, 1222, 1448, 1493, 1577, and 1612 cm^{-1} and additional visible shoulders at 1622, 1595, and 1237 cm^{-1} (topmost spectra in Figure 6a and 6b). Observed frequencies are in good agreement with the former results presented in the literature that were obtained by adsorbing pyridine on similar oxide systems.[58−61] These bands can be assigned[58,62] to the v_{15}, v_{9a}, v_{19b}, v_{19a}, v_{8b}, two v_{8a}, and v_3 modes of pyridine. Observed IR bands at ca. $1620-1600$ (v_{8a}) and ca. 1580 (v_{8b}), 1490 (v_{19a}), and 1450 (v_{19b}) cm^{-1} can be attributed to the formation of pyridine species coordinated to the surface Lewis acid sites. The weakly expressed shoulder at around 1595 cm^{-1} (in the topmost spectra in Figure 6a and 6b) is assigned to the presence of a weakly interacting pyridine species which is coordinated to the surface via hydrogen bonding. This feature almost completely disappears after increasing the annealing temperature to 373 K, in agreement with its weak interaction with the surface.

The position and multiplicity of the v_{8a} band in Figure 6a, revealing two distinct features (namely, the shoulder at 1622 cm^{-1} and the peak located at 1612 cm^{-1}), indicate the presence of two different types of Lewis acid sites. With increasing annealing temperatures, the intensities of these features as well as the feature at 1577 cm^{-1} gradually decrease. These temperature-dependent intensity changes provide valuable insight regarding the strength of the acid−base interactions between the basic pyridine probe molecule and the surface Lewis acid sites. In light of previous studies in the literature,[60,61] the band at 1577 cm^{-1} can be attributed to weak Lewis acid sites, which almost completely disappears at temperatures as low as 573 K. The band at 1612 cm^{-1} can be assigned to medium-strength Lewis acid sites whose intensity is still visible at $T > 573$ K. It is visible that the spectrum corresponding to the highest annealing temperature (723 K) is dominated by the 1622 cm^{-1} band which is associated with the strong Lewis acid sites remaining on the surface. These observations are in a good agreement, with former studies[63,64] focusing on the surface acid−base properties of γ-alumina, which suggest the presence of three different types of Lewis acid sites exhibiting distinctively dissimilar acid strengths. It was reported[63,64] that the band at ca. 1580 cm^{-1} is due to the presence of weak octahedral Al^{3+} Lewis acid sites, whereas the feature at 1612 cm^{-1} is assigned to the presence of medium-strength Lewis acid sites consisting of a pair of coordinatively unsaturated Al^{3+} ions in octahedral and tetrahedral environment, and the band at 1622 cm^{-1} was attributed to the strongest Lewis acid sites related to the presence of coordinatively unsaturated tetrahedral Al^{3+} cations.

Relatively similar temperature-dependent IR features can also be seen for the pyridine adsorption on the Ti/Al support material (Figure 6b). However, in addition to the features discussed above, an intense additional feature located at ca. 1608 cm^{-1} (partially overlapping with the band at 1612 cm^{-1}) can also be observed. With increasing annealing temperatures, this new feature becomes more discernible and shifts to higher frequencies. The thermal stability of this additional feature suggests that this IR feature is associated with the pyridine adsorption on medium-strength Lewis acid sites. Former studies[65−67] regarding pyridine adsorption on the anatase (TiO$_2$) surface reported a similar band which was associated to the Ti^{4+} Lewis acid sites with an octahedral coordination. Thus, the current spectral observations suggest that the presence of small TiO$_2$

(anatase) crystallites on the surface of the Ti/Al sample precalcined at 873 K alter the surface acidity of the alumina surface by providing additional medium-strength Lewis acid sites.

3.3.2.2. Pyridine Adsorption on the Ba/(TiO$_2$)/γ-Al$_2$O$_3$ NO$_x$ Storage System. The temperature-dependent FTIR spectra for chemisorbed pyridine dosed at 323 K on the surfaces of the Ba/Al NO$_x$ storage materials (precalcined at 873 K) with 8 and 20 wt % BaO are given in Figure 7a and 7b, respectively. In a similar fashion, Figure 8a and 8b shows the IR data corresponding to the Ti-containing samples with different BaO loadings: 8Ba/Ti/Al (a) and 20Ba/Ti/Al (b) precalcined at 873 K, respectively.

Pyridine adsorption on the surface of all of the Ba-containing samples (Figures 7 and 8) reveals characteristic features similar to the ones described above. Namely, the IR bands in the spectral regions $1640-1565$ and $1500-1100$ cm^{-1} (v_{8a}, v_{8b}, v_{19a}, v_{19b}) suggest the coordination of pyridine on the Al^{3+} Lewis acid sites, while the band at 1593 cm^{-1} indicates the presence of weakly interacting pyridine that is bound to the surface through hydrogen bonding. It should be noted that the feature corresponding to the presence of Ti^{4+} Lewis acid sites (1605 cm^{-1}) can also be seen in the case of the Ti-containing Ba/Al samples (Figure 8a and 8b). Figures 7 and 8 also clearly indicate that the presence of Ba-containing domains has a drastic influence on the Lewis acidity. This is particularly visible as a significant attenuation in the intensities of the IR signals originating from the Lewis acid sites in Figures 7 and 8, in comparison with the considerably larger IR signals observed in Figure 6, corresponding to the Ba-free samples. This observation indicates that more basic Ba-containing domains strongly interact with the acidic titania and alumina[68] domains and cover these acidic sites, which results in a decreased number of medium/strong Lewis acid sites on the binary Ba/Al and ternary Ba/Ti/Al oxide systems. These observations are in very good agreement with the formation of complex Ba−Ti and Ba−Ti−Al structures identified in the current XRD, Raman, and EDX measurements. Besides the number of Lewis acid sites, Ba-containing domains also significantly modify the strength of the surface acid sites, which is readily visible by considering the lower thermal stability of pyridine on the Ba-containing samples (Figures 7 and 8). This is also illustrated in Figure 7b, where a high Ba loading suppresses expression of the v_{8a} band (1622 and 1612 cm^{-1}) associated with the coordinatively unsaturated Al^{3+} cations from which pyridine desorption occurs at relatively low temperatures (ca. 423 K). On the other hand, Figures 7 and 8 reveal that the band at 1593 cm^{-1}, originating from the weakly interacting, hydrogen-bonded pyridine, presumably interacting predominantly with Ba domains, becomes more visible in Ba-containing samples. This suggests that the electronic environment of the Al^{3+} Lewis acid sites is profoundly altered by the Ba domains.

These results clearly illustrate that the presence of the Ba component on the surface of the pure γ-Al$_2$O$_3$ and Ti/Al sample leads to a considerable decrease in surface Lewis acidity. Furthermore, the number of remaining coordinatively unsaturated Al^{3+} and Ti^{4+} Lewis acid sites on the surface strongly depends on the Ba loading and its distribution on the surface of the Ba/Al and Ba/Ti/Al NO$_x$ storage systems.

A comparative evaluation of Figures 6−8 yields valuable information regarding the distribution of different domains on the NO$_x$ storage materials. Comparison of pyridine adsorption results on Ba/Al systems with different Ba loadings (Figure 7) point to the fact that with increasing Ba loading on the surface, the alumina surface (and their corresponding strong/medium
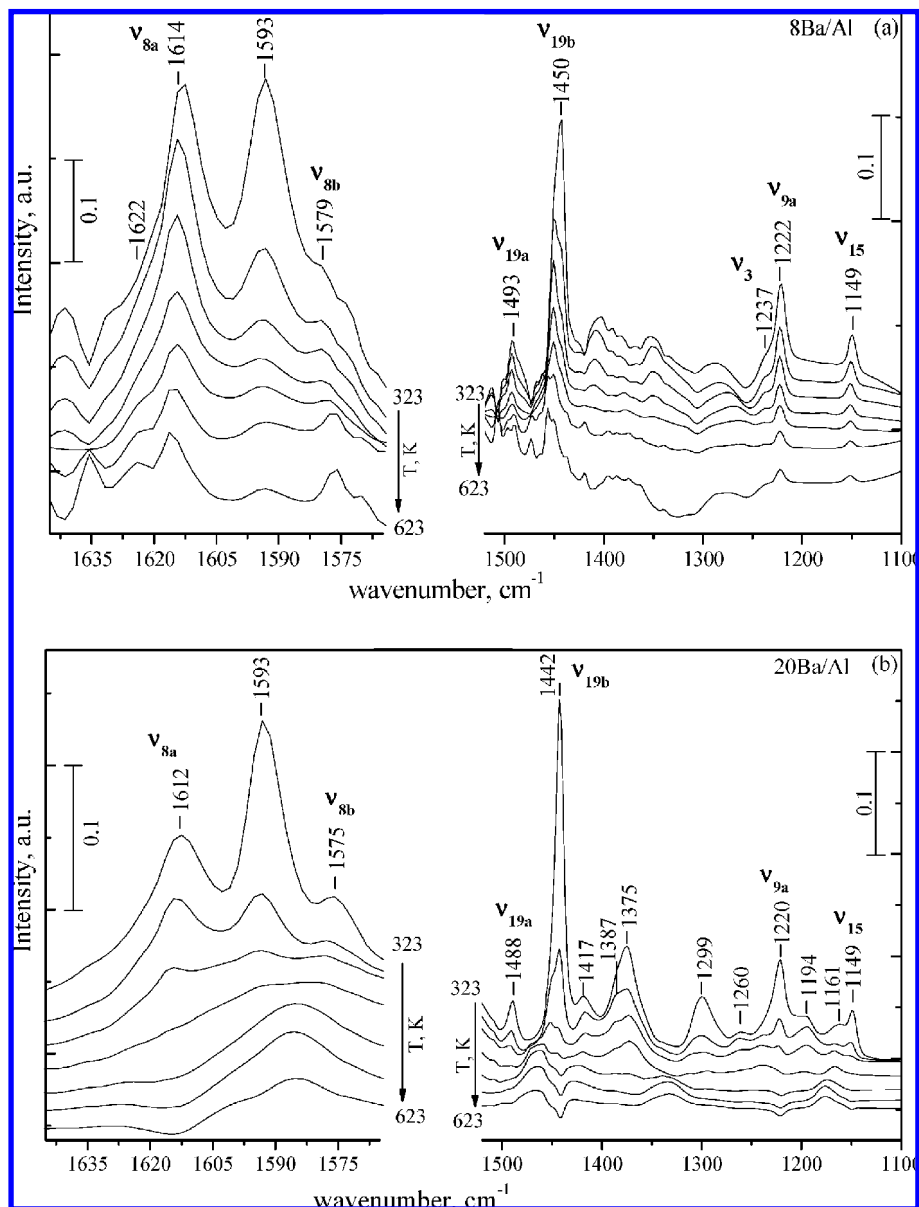
Nature of the Ti−Ba Interactions

J. Phys. Chem. C, Vol. 113, No. 25, 2009 **11023**

Figure 7. Temperature-dependent (323−723 K) FTIR spectra for chemisorbed pyridine species formed at room temperature on the surface of the Ba/Al NO_x storage materials with different BaO loadings precalcined at 873 K: (a) 8Ba/Al and (b) 20Ba/Al.

Lewis acid sites located at 1622 and 1614 cm^{-1}) is blocked by the Ba domains, resulting in a lower surface acidity where pyridine prefers to bind in a weak fashion on mostly Ba domains (1593 cm^{-1} band) through a hydrogen-bonding interaction. On the other hand, comparison of Figures 7 and 8 suggests that such a suppressive influence associated with the Ba domains on the strong/medium-strength alumina Lewis acid sites is less pronounced in the case of the Ba/Ti/Al system (Figure 8). This indicates that Ba domains prefer to interact strongly with the Ti domains rather than the alumina domains, resulting in a less pronounced suppression of the alumina-related Lewis acid sites.

Results given in Figure 8 are also in very good agreement with the current Raman and XRD data, suggesting that although 8Ba/Ti/Al sample calcined at 873 K predominantly consists of free anatase domains, on the 20Ba/Ti/Al system the strong interaction between Ba and Ti domains leads to the formation of $BaTiO_3$ at this calcination temperature. This is consistent with the suppression of the IR intensity of the Ti^{4+}-related Lewis acid sites (1605 cm^{-1}) in Figure 8b with respect to the intensity of the similar feature in Figure 8a, indicating a relative loss of

Ti^{4+} Lewis acid sites which are coordinating with the Ba domains. Along these lines, it can also be argued that in the Ba/Ti/Al system (Figure 8) Ba domains which prefer to anchor mainly on the Ti domains leave a larger fraction of free Al^{3+} sites that can be exposed to pyridine adsorption, in comparison with the Ba/Al system (Figure 7). Such dissimilarities in the Ba surface distribution in the Ba/Al and Ba/Ti/Al systems results in a higher surface acidity in the Ba/Ti/Al system.

3.2.3. SEM−EDX Measurements. Secondary electron (SE) imaging in combination with EDX analysis was used to investigate the elemental distribution of the components in the Ti/Al binary oxide support material and the Ba/Ti/Al ternary oxide NO_x storage system. Figure 9a illustrates a representative selected SEM/EDX image of the Ti/Al sample calcined at 1073 K, while Figure 9b−9e shows the SEM/EDX images corresponding to an 8Ba/Ti/Al sample, after thermal treatment at 623 K.

It can be seen in Figure 9a that the composite Ti/Al sample is characterized by an inhomogeneous elemental distribution and the segregation of Ti (red areas) and Al (green areas)
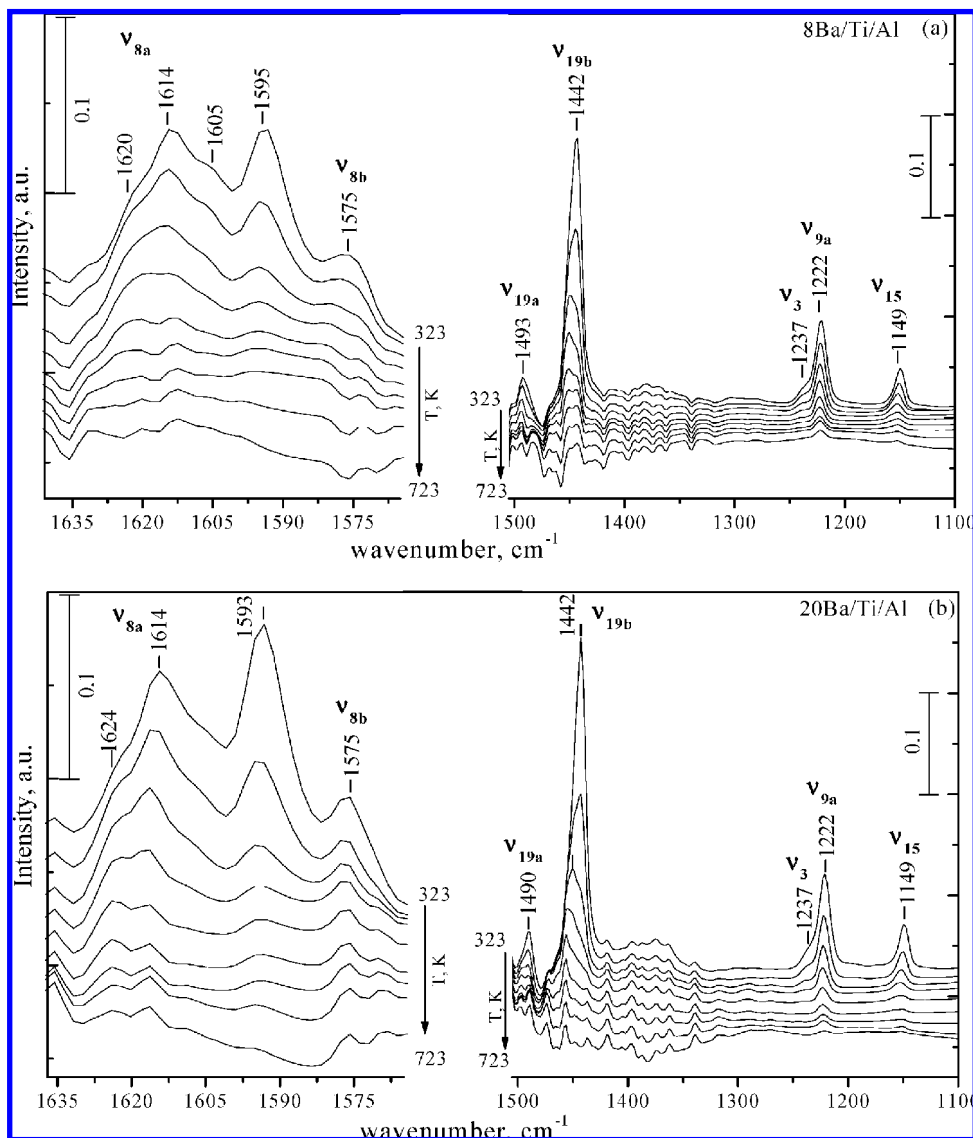
Figure 8. Temperature-dependent (323−723 K) FTIR spectra for chemisorbed pyridine species formed at room temperature on the surface of the Ba/Ti/Al ternary oxide NO_x storage materials with different BaO loadings precalcined at 873 K: (a) 8Ba/Ti/Al and (b) 20Ba/Ti/Al.

domains. On the basis of the current XRD and Raman studies (Figures 2 and 3), TiO_2 exists as an amorphous phase or in the form of a poorly crystalline anatase phase under these conditions. A similar inhomogeneous distribution of Ti was also observed in the SEM/EDX images of the Ti/Al samples calcined at lower temperatures (data not shown). It should be pointed out that the EDX technique (in the way it is used in the current work) reveals the elemental surface distribution of the system on the order of a few micrometers and does not unveil the nanometer scale dispersion of the Ti domains on the alumina surface. However, as shown below, EDX elemental mapping may still yield valuable qualitative information regarding the morphologies of different surface species.

Figure 9b−9e illustrates SEM/EDX images that belong to the same 8Ba/Ti/Al sample surface that was thermally treated at 623 K. The general morphology of the 8Ba/Ti/Al sample surface can be seen in the SEM image given in Figure 9b. Figure 9c demonstrates the EDX elemental mapping for Ti (shown in green) and Al (shown in red), indicating the inhomogeneous surface distribution of TiO_2 and Al_2O_3 domains. A similar behavior is observed when the EDX mapping of Ba and Al is examined on the same surface (Figure 9d). On the other hand, Figure 9e displays a very striking observation. In Figure 9e,

EDX mapping for Ba and Ti domains is shown in red and green, respectively. Interestingly, the EDX map is dominated by the yellow domains rather than green or red domains, indicating the presence of a combination signal originating from the spatial overlap of Ba and Ti signals. Considering the spatial resolution of the EDX signal which is on the order of a few micrometers, observation of a predominant yellow signal suggests that Ti and Ba elements form spatially overlapping domains in the submicrometer scale that are in the form of $Ba(NO_3)_2/TiO_2$, BaO/TiO_2, and/or $Ba_xTi_yO_z$. This observation is in very good agreement with the current Raman and XRD data, indicating a very high affinity of Ti domains toward Ba-containing surface species. It is worth mentioning that EDX data reveal that the high affinity of the Ti domains toward Ba-containing species is present in both 8Ba/Ti/Al and 20Ba/Ti/Al systems at a variety of temperatures within 423−1073 K (data not shown). Figure 9b−9e also indicates that TiO_2 sites present strong anchoring sites for the NO_x storage component in the Ba/Ti/Al system and hence modify the stability of the stored nitrates by altering the interfacial interaction between the Ba-containing sites and its underlying support surface. This observation is also in line with the current XRD, Raman, and IR data (Figures 4, 5, and
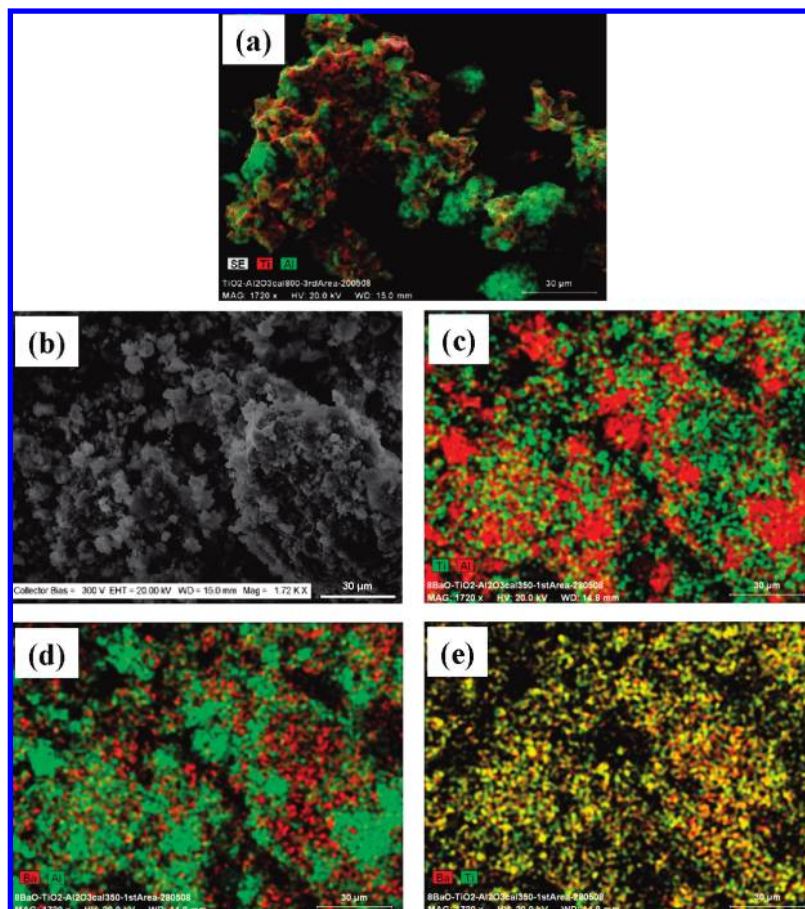
Nature of the Ti—Ba Interactions

J. Phys. Chem. C, Vol. 113, No. 25, 2009 **11025**

Figure 9. Selected SEM/EDX images for Ti/Al and Ba/Ti/Al samples. (a) Overlapping SEM image and Ti + Al elemental EDX mapping for the Ti/Al sample calcined at 1073 K. Images given in b—e correspond to the same 8Ba/Ti/Al sample calcined at 623 K. (b) SEM image, (c) Ti + Al, (d) Ba + Al, (e) Ba and Ti EDX mapping images.

8), revealing facile solid-state reactions between Ti and Ba domains at higher temperatures on the Ba/Ti/Al system.

4. Summary and Conclusions

Fundamental understanding of the interactions between the catalytic components of complex NO_x storage materials is crucial for designing new materials with improved catalytic properties. Along these lines, we systematically examined the thermal evolution of a Ti/Al binary oxide support material in comparison with a Ba/Ti/Al ternary oxide NO_x storage material and obtained significant insights regarding the surface species that exist on the Ba/Ti/Al system at different temperatures. This fundamental knowledge is particularly essential for a molecular understanding of the sulfur tolerance effect of TiO_2 in NSR systems. The main results of the current work can be summarized as follows:

(a) The sol—gel-synthesized composite TiO_2/γ-Al_2O_3 binary oxide exhibits a relatively high thermal stability, where the presence of γ-Al_2O_3 suppresses the anatase-to-rutile phase transformation at $T \leq 1073$ K. At higher temperatures such as 1273 K, formation of rutile as well as α-Al_2O_3 was observed.

(b) For the 20Ba/Ti/Al system, completion of the nitrate decomposition process occurred at a temperature that is about 250 K lower than that of the 20Ba/Al system. This can be attributed to a weaker interaction between the NO_x storage component (i.e., $Ba(NO_3)_2$) and the γ-alumina surface and a stronger TiO_2—$Ba(NO_3)_2$ interaction.

(c) In the Ba/Ti/Al system, Ti-containing domains present a high affinity toward Ba-containing domains. This is evident by the observation of spatially overlapping Ti and Ba signals

detected in the EDX imaging experiments as well as the presence of complex Ti—Ba mixed structures identified in the Raman and XRD experiments.

(d) The studied NO_x storage systems exhibited different surface acidity. The presence of Ti-containing domains on the investigated oxide surfaces yielded additional medium-strength Lewis acid sites, whereas the presence of Ba domains decreased both the number and the strength of the surface Lewis acid sites.

(e) In the Ba/Ti/Al system, strong interaction between Ti- and Ba-containing domains results in significant surface reactions above 873 K where formation of $BaTiO_3$, $Ba_{1.23}Al_{2.46}Ti_{5.54}O_{16}$ and possibly $BaTi_2O_5$ and/or a complex $Ba_xAl_yTi_zO_n$ phase is observed. The Ba content of the Ba/Ti/Al system was also found to be a determining factor on the relative abundances of the observed high-temperature species. At 1273 K, 8Ba/Ti/Al sample revealed the presence of Ti-containing domains mostly in the form of anatase, while 20Ba/Ti/Al sample was dominated by the $Ba_{1.23}Al_{2.46}Ti_{5.54}O_{16}$ phase. These high-temperature species can also shed some light on the possible surface species that can be formed upon thermal aging of complex NO_x storage reduction catalysts.

References and Notes

(1) Toyota Patent. European Patent Application no. 0573 672A1, 1992.

(2) Takahashi, N.; Shinjoh, H.; Iijima, T.; Suzuki, T.; Yamazaki, K.; Youkota, K.; Suzuki, H.; Miyoshi, N.; Matsumoto, S.; Tanizam, T.; Tanaka, T.; Tateishi, S.; Kasahara, K. *Catal. Today* **1996**, *27*, 63.

(3) Rohr, F.; Peter, S. D.; Lox, E.; Kögel, M.; Sassi, A.; Juste, L.; Rigaudeau, C.; Belot, G.; Gélin, P.; Primet, M. *Appl. Catal., B* **2005**, *56*, 201.

(4) Takeuchi, M.; Matsumoto, S. *Top. Catal.* **2004**, *28*, 151.

(5) Epling, W. S.; Parks, J. E.; Campbell, G. C.; Yezerets, A.; Currier, N. W.; Campbell, L. E. *Catal. Today* **2004**, *96*, 21.

(6) Epling, W. S.; Campbell, L. E.; Yezerets, A.; Currier, N. W.; Parks, J. E., II *Catal. Rev.* **2004**, *46*, 163.

(7) Lietti, L.; Forzatti, P.; Nova, I.; Tronconi, E. *J. Catal.* **2001**, *204*, 175.

(8) Nova, I.; Castoldi, L.; Lietti, L.; Tronconi, E.; Forzatti, P. *Catal. Today* **2002**, *75*, 431.

(9) Fridell, E.; Persson, H.; Westerberg, B.; Olsson, L.; Skoglundh, M. *Catal. Lett.* **2000**, *66*, 71.

(10) Ozensoy, E.; Peden, C. H. F.; Szanyi, J. *J. Catal.* **2006**, *243*, 149.

(11) Ozensoy, E.; Szanyi, J.; Peden, C. H. F. *J. Phys. Chem. B* **2006**, *110*, 17–001.

(12) Ozensoy, E.; Szanyi, J.; Peden, C. H. F. *J. Phys. Chem. B* **2005**, *110*, 17–009.

(13) Ozensoy, E.; Szanyi, J.; Peden, C. H. F. *J. Phys. Chem. B* **2005**, *109*, 3431.

(14) Ozensoy, E.; Szanyi, J.; Peden, C. H. F. *J. Phys. Chem. B* **2005**, *109*, 15–977.

(15) Ozensoy, E.; Szanyi, J.; Peden, C. H. F. *J. Phys. Chem. B* **2005**, *110*, 8025.

(16) Staudt, T.; Desikusumastuti, A.; Happel, M.; Vesselli, E.; Baraldi, A.; Gardonio, S.; Lizzit, S.; Rohr, F.; Libuda, J. *J. Phys. Chem. C* **2008**, *112*, 9835.

(17) Olsson, L.; Fridell, E. *J. Catal.* **2002**, *210*, 340.

(18) Olsson, L.; Andersson, B. *Top. Catal.* **2004**, *28*, 89.

(19) Matsumoto, S.; Kazuaki, S.; Shinji, T.; Yasuo, I. *Catalysts Catal.* **2000**, *42*, 65.

(20) Chang, J.-R.; Chang, S. L.; Lin, T.-B. *J. Catal.* **1997**, *169*, 338.

(21) Matsumoto, S.; Ikeda, Y.; Suzuki, H.; Ogai, M.; Miyoshi, N. *Appl. Catal., B* **2000**, *25*, 115.

(22) Uy, D.; Wiegand, K. A.; O'Neill, A. E.; Dearth, M. A.; Weber, W. H. *J. Phys. Chem. B* **2002**, *106*, 387.

(23) Wei, X.; Liu, X.; Deeba, M. *Appl. Catal., B* **2005**, *58*, 41.

(24) Hirata, H.; Hachisuka, I.; Ikeda, Y.; Tsuji, S.; Matsumoto, S. *Top. Catal.* **2001**, *16/17*, 145.

(25) Yamamoto, K.; Kikuchi, R.; Takeguchi, T.; Eguchi, K. *J. Catal.* **2006**, *238*, 449.

(26) Suzuki, H.; Muramoto, R.; Takahashi, N. *Toyota Tech. Rev.* **1996**, *46*, 68.

(27) Imagawa, H.; Tanaka, T.; Takahashi, N.; Matsunaga, S.; Suda, A.; Shinjoh, H. *Appl. Catal., B* **2009**, *86*, 63.

(28) Liu, Y.; Meng, M.; Zou, X.; Li, X.; Zha, Y. *Catal. Commun.* **2008**, *10*, 173.

(29) Liu, Y.; Meng, M.; Li, X.-G.; Guo, L.-H.; Zha, Y.-Q. *Chem. Eng. Res. Des.* **2008**, *86*, 932.

(30) Takahashi, N.; Suda, A.; Hachisuka, I.; Sugiura, M.; Sobukawa, H.; Shinjoh, H. *Appl. Catal., B* **2007**, *72*, 187.

(31) Kantcheva, M. M.; Hadjiivanov, K. I.; Klissurski, D. G. *J. Catal.* **1992**, *134*, 299.

(32) de Boer, J. H.; Linsen, B. G.; van der Plas, Th.; Zondervan, G. J. *J. Catal.* **1965**, *4*, 649.

(33) Hang, C. H.; Gopalan, R.; Lin, Y. S. *J. Membr. Sci.* **1994**, *91*, 27.

(34) Yang, J.; Huang, Y. X.; Ferreira, J. M. F. *J. Mater. Sci. Lett.* **1997**, *16*, 1933.

(35) Orendorz, A.; Brodyanski, A.; Lösch, A.; Bai, L. H.; Chen, Z. H.; Le, Y. K.; Ziegler, C.; Gnaser, H. *Surf. Sci.* **2007**, *601*, 4390.

(36) Su, W.; Zhang, J.; Feng, Zh.; Chen, T.; Ying, P.; Li, C. *J. Phys. Chem. C* **2008**, *112*, 7710.

(37) Oshaka, T.; Izumi, F.; Fujiki, Y. *J. Raman Spectrosc.* **1978**, *7*, 321.

(38) Bersani, D.; Lottici, P. P.; Ding, X.-Z. *Appl. Phys. Lett.* **1998**, *72*, 73.

(39) Zhang, Y.-H.; Chan, C. K.; Porter, J. F.; Guo, W. *J. Mater. Res.* **1998**, *13*, 2602.

(40) Bersani, D.; Antonioli, G.; Lottici, P. P.; Lopez, T. *J. Non-Cryst. Solids* **1998**, *232–234*, 175.

(41) Bersani, D.; Lottici, P. P.; Ding, X. Z. *Appl. Phys. Lett.* **1998**, *72*, 73.

(42) Zhnag, W. X.; Wang, C. B.; Lien, H. L. *Catal. Today* **1998**, *40*, 387.

(43) Kumar, K. N. P.; Keizer, K.; Burggraff, A. J.; Okubo, T.; Nagomoto, H.; Morooka, S. *Nature* **1992**, *358*, 48.

(44) Wang, Z.; Deng, X. *Mater. Sci. Eng., B* **2007**, *140*, 109.

(45) Fisher, J. G.; Lee, B.-K.; Choi, S.-Y.; Wang, S.-M.; Kang, S.-J. L. *J. Eur. Ceram. Soc.* **2006**, *26*, 1619.

(46) Andonova, S. M.; Kayhan, E. ; Şentürk, G. S.; Chusuei, Ch.C.; Ozensoy, E. Submitted for publication, 2008.

(47) Mestl, G.; Rosynek, M. P.; Lunsford, J. H. *J. Phys. Chem. B* **1997**, *101*, 9321.

(48) Mestl, G.; Rosynek, M. P.; Lunsford, J. H. *J. Phys. Chem. B* **1997**, *101*, 9329.

(49) Hess, Ch.; Lunsford, J. H. *J. Phys. Chem. B* **2003**, *107*, 1982.

(50) Hess, Ch.; Lunsford, J. H. *J. Phys. Chem. B* **2002**, *106*, 6358.

(51) Mestl, G.; Rosynek, M. P.; Lunsford, J. H. *J. Phys. Chem. B* **1998**, *102*, 154.

(52) Szailer, T.; Kwak, J. H.; Kim, D. H.; Szanyi, J.; Wang, Ch.; Peden, C. H. F. *Catal. Today* **2006**, *114*, 86.

(53) Szanyi, J.; Kwak, J. H.; Kim, D. H.; Burton, S. D.; Peden, C. H. F. *J. Phys. Chem. B* **2005**, *109*, 27.

(54) Kwak, J. H.; Kim, D. H.; Szailer, T.; Peden, C. H. F.; Szanyi, J. *Catal. Lett.* **2006**, *111*, 119.

(55) Szanyi, J.; Kwak, J. H.; Hanson, J.; Wang, C.; Szailer, T.; Peden, C. H. F. *J. Phys. Chem. B* **2005**, *109*, 7339.

(56) Hadjiivanov, K. *Catal. Rev.-Sci. Eng.* **2000**, *42*, 71.

(57) Li, J.; Zhu, Y.; Ke, R.; Hao, J. *Appl. Catal., B* **2008**, *80*, 202.

(58) Kim, S.; Wang, X.; Buda, C.; Neurock, M.; Koper, O. B.; Yates, J. T., Jr. *J. Phys. Chem. C* **2009**, *113*, 2219.

(59) Healy, M. H.; Wieserman, L. F.; Arnett, E. M.; Wefers, K. *Langmuir* **1989**, *5*, 114.

(60) Morterra, C.; Chiorino, A.; Ghiotti, G.; Garrone, E. *J. Chem. Soc., Faraday Trans.* **1979**, *75*, 271.

(61) Abbattista, F.; Delmastro, S.; Gozzelino, G.; Mazza, D.; Vallino, M.; Busca, G.; Lorenzelli, V.; Ramis, G. *J. Catal.* **1989**, *117*, 42.

(62) Kline, C.H.Jr.; Turkevich, J. *J. Chem. Phys.* **1944**, *12*, 300.

(63) Haneda, M.; Joubert, E.; Menezo, J.-Ch.; Duprez, D.; Barbier, J.; Bion, N.; Daturi, M.; Saussey, J.; Lavalley, J.-C.; Hamada, H. *Phys. Chem. Chem. Phys.* **2001**, *3*, 1366.

(64) Lundie, D. T.; Mclnroy, A. R.; Marshall, R.; Winfield, J. M.; Jones, P.; Dudman, C. C.; Parker, S. F.; Mitchell, C.; Lennon, D. *J. Phys. Chem. B* **2005**, *109*, 11592.

(65) Kooli, F.; Sasaki, T.; Watanabe, M.; Martin, C.; Rives, V. *Langmuir* **1999**, *15*, 1090.

(66) Bezrodna, T.; Puchkovska, G.; Shimanovska, V.; Chashechnikova, I.; Khalyavka, T.; Baran, J. *Appl. Surf. Sci.* **2003**, *214*, 222.

(67) Li, J.; Zhu, Y.; Ke, R.; Hao, J. *Appl. Catal., B:Environ.* **2008**, *80*, 202.

(68) Kwak, J. H.; Hu, J. Z.; Kim, D. H.; Szanyi, J.; Peden, C. H. F. *J. Catal.* **2007**, *251*, 189.